ChemComm

COMMUNICATION

View Article Online
View Journal | View Issue

Cite this: *Chem. Commun.*, 2024, **60**, 8900

Received 6th June 2024,
Accepted 20th July 2024

DOI: 10.1039/d4cc02753a

rsc.li/chemcomm

Enhanced CO_2 conversion in dielectric barrier discharge plasma coupled with a heterojunction photocatalyst†

Xiao Feng,[a] Lefei Cao,[b] Chengfan Fu,[b] Fei Qi,*[b] Nan Zhang,[b] Yayun Pu,[b] Zhiyu Liang,[b] Xiaosheng Tang *[ab] and Qiang Huang *[b]

$CsPbBr_3$ quantum dots were grown on ReS_2 nanosheets to form $CsPbBr_3$@ReS_2 heterojunctions using an anti-solvent method. The composition, morphology, spatial distribution, and optical absorption of samples were characterized. $CsPbBr_3$@ReS_2-15 exhibits not only a higher photocatalytic performance than $CsPbBr_3$ due to the improved optical absorption and Z-scheme charge migration, but also a higher CO_2 conversion ratio (35.60%) and energy efficiency (13.10%) in the dielectric barrier discharge (DBD) plasma due to superior photocatalytic activity, increased micro-discharge time, and improved discharge uniformity. This work provides a strategy for plasma photocatalytic CO_2 conversion.

Conversion of CO_2 into high value-added chemicals and fuels *via* renewable green electricity is becoming increasingly pressing because promising potential exists to resolve the greenhouse effect and energy crisis problems.[1,2] CO_2 molecules are inert and possess ultra-high thermal stability, requiring the energy of 750 kJ mol^{-1} to disintegrate the carbon–oxygen double bond, which leads to significant challenges for the traditional thermal approach to CO_2 decomposition.[3] Non-thermal plasma (NTP) is considered a promising alternative for reducing CO_2 gases into syngas or other valuable chemicals at mild temperatures.[4] At present, various NTP methods have been proven to convert CO_2 into CO, including dielectric barrier discharge (DBD),[5] corona discharge,[6] glow discharge,[7] microwave discharge,[8] gliding arc,[9] and radio-frequency plasma.[10] It is advantageous to use DBD plasma because it is affordable, and it can produce a high electron density. Thus far, DBD plasma has been widely used for CO_2 conversion, and previous reports indicate that packing materials in the DBD plasma reactor can increase the CO_2 conversion efficiency.[6] In fact, during CO_2 conversion *via* the DBD plasma approach, there are many high-energy electrons and ultraviolet-visible photons that can stimulate the photocatalysis process. Therefore, it is significant to exploit suitable photocatalysts as packing materials to enhance the CO_2 conversion efficiency for DBD plasma.

There has recently been great interest in halide perovskites, such as $CsPbBr_3$, in photocatalytic fields due to their wide range of visible light absorption and high absorption coefficient.[11] However, the low separation and high recombination rate of photoexcited carriers leads to low CO_2 conversion efficiency for $CsPbBr_3$.[12] Fortunately, the construction of a heterojunction is proposed to break through these issues. The combination of $CsPbBr_3$ with two-dimensional (2D) semiconductors to form a heterojunction is a potential strategy to increase the CO_2 photoreduction efficiency, because 2D semiconductors usually have a large specific area, abundant active sites, and short distance of charge transportation.

ReS_2, one member of 2D semiconductors, presents the outstanding optoelectronic properties of direct bandgap, strong optical absorption, and ultra-high optical responsivity. Therefore, it is meaningful to build a heterojunction of $CsPbBr_3$ and ReS_2 to increase the CO_2 photoreduction efficiency. Additionally, it is also beneficial to prepare a porous heterostructure of $CsPbBr_3$ and ReS_2. The porous structure has the advantages of a large specific surface area and abundant surface topographies to increase the CO_2 photoreduction.[13] The porous photocatalysts in DBD plasma can create micro-discharges in the pores, which in turn change the local electric field strength and discharge type of the plasma, affecting CO_2 conversion reactions. Porous surfaces can adsorb active excited species generated during the plasma discharge, thus increasing the residence time of active species and facilitating surface catalytic reactions.[14] To the best of our knowledge, the construction of a $CsPbBr_3$@ReS_2 heterojunction with a porous surface structure has not been previously reported.

In this work, $CsPbBr_3$ quantum dots (QDs) were grown *in situ* on porous ReS_2 microspheres to form a $CsPbBr_3$@ReS_2 heterojunction. Due to the increased optical absorption and enhanced separation of photogenerated carriers, the CO_2

[a] *State Key Laboratory of Power Transmission Equipment Technology, Chongqing University, Chongqing 400044, China. E-mail: xstang@cqu.edu.cn*
[b] *School of Optoelectronic Engineering, Chongqing University of Posts and Telecommunications, Chongqing 400065, China. E-mail: huangqiang@cqupt.edu.cn, qifei@cqupt.edu.cn*

† Electronic supplementary information (ESI) available. See DOI: https://doi.org/10.1039/d4cc02753a

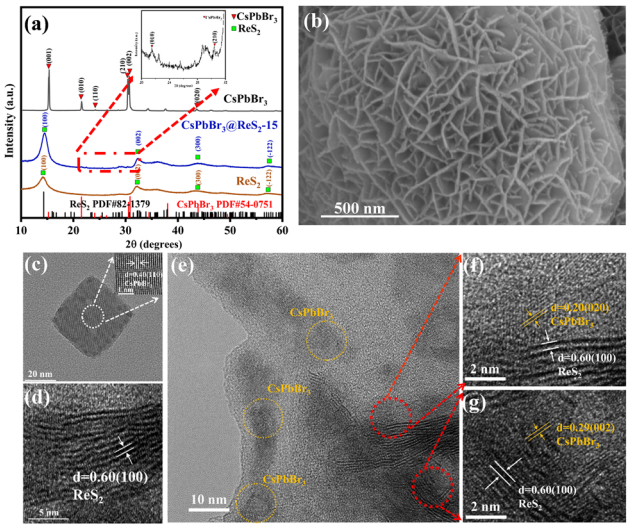

Fig. 1 (a) XRD patterns of $CsPbBr_3$, ReS_2, and $CsPbBr_3$@ReS_2; (b) SEM image of ReS_2; HRTEM images of (c) $CsPbBr_3$, (d) ReS_2, and (e)–(g) $CsPbBr_3$@ReS_2. The inset in (c) shows an enlarged HRTEM image of $CsPbBr_3$.

photoreduction efficiency of $CsPbBr_3$@ReS_2 is higher than that of pristine $CsPbBr_3$. $CsPbBr_3$@ReS_2 heterojunction photocatalysts were used to increase the CO_2 conversion ratio and energy efficiency in DBD plasma, which benefitted from the synergistic conversion of CO_2 by the DBD plasma and heterojunction photocatalyst. This work provides guidance for future designs of plasma photocatalytic systems for efficient CO_2 conversion.

The sample preparation details are shown in the Experimental section (ESI†). Fig. 1a shows the X-ray diffraction (XRD) patterns of $CsPbBr_3$, ReS_2, and $CsPbBr_3$@ReS_2-15. The XRD peaks of $CsPbBr_3$ QDs at 15.3°, 21.6°, 24.1°, 30.4°, 30.7°, and 43.6° were attributed to the (001), (010), (110), (210), (002), and (020) planes, respectively, and were consistent with the standard card PDF #54-0751. XRD peaks corresponding to the (100), (002), (300), and (−122) planes were detected for ReS_2 microspheres. Obvious XRD peaks for ReS_2 were observed for $CsPbBr_3$@ReS_2-15, while weak XRD peak signals at 21.6° and 30.4° belonging to the (010) and (210) planes of $CsPbBr_3$ were also detected, which were due to the low content and small size of $CsPbBr_3$. A scanning electron microscopy (SEM) image of prepared ReS_2 revealed a microsphere structure (Fig. 1b). Additionally, there were many flakes and holes on the microsphere surface, which are favorable for anchoring $CsPbBr_3$ QDs and absorbing CO_2 molecules.

In the high-resolution transmission electron microscopy (HRTEM) image in Fig. 1c, the $CsPbBr_3$ QDs exhibited a cubic shape and lattice spacing of 0.40 nm. The ReS_2 flake in Fig. 1d presents a few layers with a lattice distance of 0.60 nm corresponding to the (100) plane. Fig. 1e shows that $CsPbBr_3$ QDs are anchored on the ReS_2 surface for $CsPbBr_3$@ReS_2-15. Compared with the pristine $CsPbBr_3$ QDs, the size of $CsPbBr_3$ QDs on ReS_2 decreases, and the corresponding shape changes into an irregular structure, which may induce more catalytic active sites because of a higher surface volume ratio. Fig. 1f and g shows the HRTEM images corresponding to the red circle regions in Fig. 1e. It is observed that the (020) plane with a lattice spacing of 0.2 nm and the (002) plane with a lattice spacing of 0.29 nm for $CsPbBr_3$ adjoin the (100) plane with a lattice spacing of 0.60 nm for ReS_2, verifying the formation of a $CsPbBr_3$@ReS_2 heterojunction. In addition, the energy dispersive spectroscopy (EDS) elemental mapping (Fig. S1, ESI†) shows that there is adequate overlap of Cs, Pb, Br, Re, and S elements.

The surface chemical states and interfacial interactions were investigated by X-ray photoelectron spectroscopy (XPS) analysis. The XPS full spectrum (Fig. 2a) verified the presence of Cs, Pb, Br, Re, and S elements in $CsPbBr_3$@ReS_2-15. Compared to the pristine $CsPbBr_3$, the Cs 3d spectrum of $CsPbBr_3$@ReS_2-15 (Fig. 2b) exhibited two XPS peaks at 737.79 and 723.82 eV corresponding to Cs $3d_{3/2}$ and Cs $3d_{5/2}$, respectively, which were not significantly shifted. However, the Pb 4f (Fig. 2c) and Br 3d (Fig. 2d) binding energies were redshifted by 1.20 and 0.23 eV, respectively. In contrast, the Re 4f (Fig. 2e) and S 2p (Fig. 2f) binding energies of $CsPbBr_3$@ReS_2-15 showed the opposite trend, whereby the Re 4f and S 2p peaks were blueshifted by 1.00 and 0.68 eV, respectively. A higher electron binding energy indicates a decrease in electron density, while a lower electron binding energy indicates an increase in electron density. Consequently, the XPS results denote electron transfer from ReS_2 to $CsPbBr_3$ within the $CsPbBr_3$@ReS_2 heterojunction, indicating the intimate interfacial contact and robust chemical interaction between $CsPbBr_3$ and ReS_2. Fig. S2 (ESI†) shows that $CsPbBr_3$@ReS_2 has a lower photoluminescence (PL) intensity than that of $CsPbBr_3$, demonstrating the increased separation of photogenerated carriers due to the heterojunction.

To obtain the band structure, UV-vis spectra and valence band (VB) XPS spectra were obtained. The optical absorption edges of pristine $CsPbBr_3$ and ReS_2 are about 544 and 805 nm in Fig. S3a (ESI†), respectively, suggesting their wide light absorption range. According to the inset in Fig. S3a (ESI†), the optical absorption ability of $CsPbBr_3$@ReS_2-15 is stronger compared to $CsPbBr_3$ and ReS_2, which may be due to the strong electron coupling between $CsPbBr_3$ and ReS_2, indicating the promising capacity of solar light utilization. In addition, Fig. S3b (ESI†) presents the Tauc plots of $CsPbBr_3$ and ReS_2, from which the bandgap energy (E_g) of 2.30 and 1.57 eV was determined for $CsPbBr_3$ and ReS_2, respectively. Meanwhile, the VB positions of $CsPbBr_3$ and ReS_2 are respectively confirmed to be 1.03 and 1.25 eV, as shown in Fig. S4 (ESI†). Then, the conduction band (CB) positions (E_g = CB − VB) of $CsPbBr_3$ and ReS_2 are calculated to be −1.27 eV and −0.32 eV, respectively.

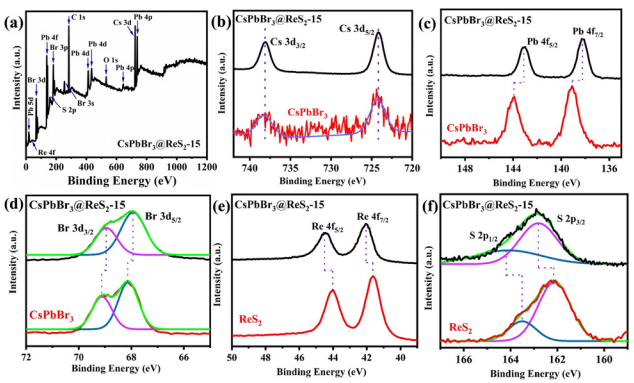

Fig. 2 (a) XPS full spectrum of $CsPbBr_3$@ReS_2-15. High-resolution XPS spectra of (b) Cs 3d, (c) Pb 4f, and (d) Br 3d of (e) Re 4f and (f) S 2p.

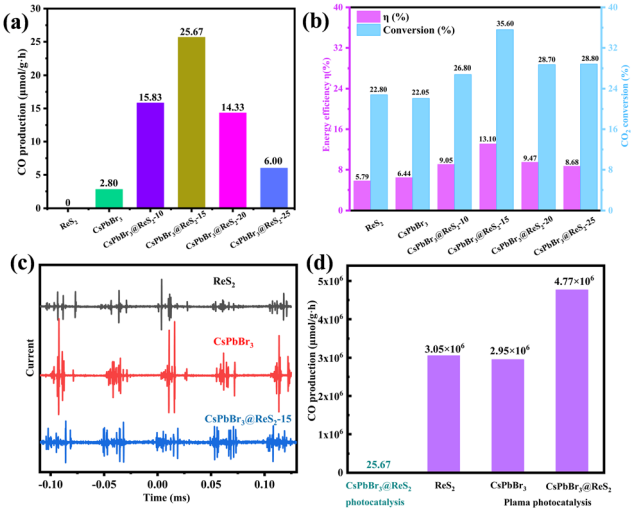

Fig. 3 (a) Photocatalysis, (b) plasma photocatalysis performances, and (c) discharge current of ReS_2, $CsPbBr_3$, and $CsPbBr_3$@ReS_2; (d) CO yield of $CsPbBr_3$@ReS_2 photocatalysis, ReS_2 plasma catalysis, and plasma photocatalysis of $CsPbBr_3$ and CsPbBr3@ReS_2.

Especially, it is noted that the band structure of ReS_2 does not match with the reduction potential (−0.52 V) of CO_2 conversion to CO, which agrees with the result of the CO_2 photoreduction for ReS_2 in Fig. 3a. However, the band alignment of the $CsPbBr_3$@ReS_2 heterojunction meets the requirements for CO_2 conversion to CO, as shown in Fig. S3c (ESI†). $CsPbBr_3$@ReS_2 presents increased photocatalytic efficiency of CO_2 reduction as compared to that of $CsPbBr_3$ and ReS_2 in Fig. 3a. The traditional type II heterojunction mechanism cannot reasonably explain the principle of charge carrier transfer and photocatalytic CO_2 reduction for $CsPbBr_3$@ReS_2-15. Therefore, a Z-type charge flow path is proposed for $CsPbBr_3$@ReS_2-15. As a result, the photogenerated carrier separation efficiency of ReS_2 and $CsPbBr_3$ in the heterostructure is enhanced, improving the CO_2 photoreduction performance.[15,16] Additionally, the main CO_2 photoreduction processes for $CsPbBr_3$@ReS_2 are summarized as reaction Formulas S1–S4 (ESI†).

To examine the photocatalytic performance of samples, the products of CO_2 photoreduction were tested. In Fig. 3a, after 3 h of continuous light irradiation, all samples showed 100% selectivity for CO, while $CsPbBr_3$ possessed low activity (CO yield = 2.80 μmol g^{-1} h^{-1}). Additionally, ReS_2 does not show CO_2 photoreduction ability, which is consistent with the band arrangement structure of ReS_2. However, when $CsPbBr_3$ is anchored on ReS_2, the CO_2 photoreduction performance is greatly enhanced. Particularly, the largest CO yield (25.67 μmol g^{-1} h^{-1}) was for $CsPbBr_3$@ReS_2-15, and was 9.17-fold higher than that of $CsPbBr_3$ (2.80 μmol g^{-1} h^{-1}). Because coupling with ReS_2 had a significant role in the photocatalytic performance of $CsPbBr_3$, the effects of the molar ratio of $CsPbBr_3$ to ReS_2 in the heterojunction on the photocatalytic activity were further investigated. Compared to $CsPbBr_3$@ReS_2-15 (25.67 μmol g^{-1} h^{-1}), the CO production of $CsPbBr_3$@ReS_2-20 (14.33 μmol g^{-1} h^{-1}) and $CsPbBr_3$@ReS_2-25 (6.00 μmol g^{-1} h^{-1}) clearly decreased, which occurred because the excess ReS_2 impeded effective utilization of the photon energy due to a lack of photocatalytic activity for CO_2 reduction by pristine ReS_2.

In DBD plasma, electrons are subjected to an applied electric field and gain sufficient energy to obtain high velocity. Afterwards, the high-energy electrons collide with the gas molecules in the discharge gap, resulting in gas ionization, which triggers an electron avalanche.[17] In addition to elastic collisions, inelastic collisions also occur in the plasma to produce many active species, which can be involved in a range of chemical reactions. More importantly, CO_2 molecules can be activated and enter into vibrationally excited states CO_2^{V*} in plasma to decrease the reaction barrier to CO_2 reduction.[18] Therefore, it is significant to employ the active state CO_2^{V*} in DBD plasma to induce photocatalytic CO_2 conversion.

The plasma photocatalytic CO_2 reduction performances for ReS_2, $CsPbBr_3$, and $CsPbBr_3$@ReS_2 with different molar ratios are shown in Fig. 3b, and the test details are described in the ESI.† It is found that the plasma photocatalytic performance of $CsPbBr_3$@ReS_2 is higher than that of ReS_2 and $CsPbBr_3$. $CsPbBr_3$@ReS_2-15 exhibits the highest CO_2 conversion (35.60%) and energy efficiency (13.10%), which is attributed to the optimal photocatalytic activity, as shown in Fig. 3a. Moreover, the porous surface structure of ReS_2 results in increased residence time of CO_2 molecules in the reaction region[19] and increases the chance of collisions between electrons and CO_2. This explains the higher CO_2 conversion in DBD plasma filled with ReS_2 (22.80%) compared to $CsPbBr_3$ (22.05%). In contrast, the energy efficiency of the plasma filled with ReS_2 was slightly lower than that of the plasma filled with $CsPbBr_3$, which may be due to the higher energy input per CO_2 molecule, resulting in a decreasing trend in energy utilization efficiency.[20]

The reasons for performance differences were further explored by measuring the discharge characteristics and charge properties of DBD plasma. The total current consists of both conduction current and displacement current. Conduction current is formed by the directional movement of charged particles in the plasma under the influence of an electric field. The charge characteristics such as lifetime and discharge intensity can be determined by conduction current. In fact, filling the DBD plasma with catalyst is expected to reduce the amplitude of the current peak and cause a change in the discharge modes. Usually, filamentary discharge mainly occurs between particles or between particles and wall surfaces, while surface discharge mainly exists on the surface of the catalyst. Compared with regularly shaped catalysts, filling materials with a porous structure are more likely to cause surface discharge.[13]

It is observed that the discharge current amplitude of DBD plasma filled with ReS_2 and $CsPbBr_3$@ReS_2-15 is lower than that of $CsPbBr_3$, as shown in Fig. 3a. This is consistent with previous works demonstrating that DBD plasma packed with $BaTiO_3$,[5] glass beads,[5] or Ni/Al_2O_3[21] significantly reduced the current amplitude. Furthermore, $CsPbBr_3$@ReS_2-15 increases the micro-discharge time, which is the time of the continuous plasma discharge during a discharge period, compared with ReS_2 and $CsPbBr_3$ (Fig. 3a), implying that a heterogenous photocatalyst improves the plasma discharge characteristics. The uniformity of the plasma discharge for $CsPbBr_3$@ReS_2-15 is optimal, which is beneficial for plasma-driven CO_2 conversion. In addition, the amounts of the peak-to-peak charge (Q_{pk-pk}) and discharge charge (Q_d) are also one of the indicators of the actual reaction (Fig. S5, ESI†). DBD plasma with

$CsPbBr_3$@ReS_2-15 holds the largest Q_{pk-pk} (545 nC) and Q_d (290 nC) compared with $CsPbBr_3$ (Q_{pk-pk} = 500 nC, Q_d = 250 nC) and ReS_2 (Q_{pk-pk} = 530 nC, Q_d = 280 nC) (Fig. S6, ESI†), which indicates that the physical and chemical reactions in the DBD plasma filled with $CsPbBr_3$@ReS_2-15 are the most violent for CO_2 conversion.

Furthermore, according to the optical absorption spectrum of $CsPbBr_3$@ReS_2-15 (inset of Fig. S3a, ESI†) and optical emission spectrum of DBD plasma filled with $CsPbBr_3$@ReS_2-15 (Fig. S7, ESI†), the photons generated in the plasma can be absorbed by the photocatalyst for CO_2 conversion.[22] In fact, the vibrationally excited CO_2 molecules in the plasma can be absorbed on the photocatalyst surface to reduce the potential barrier for the subsequent reduction process, which facilitates the "state-to-state catalytic chemistry" so that high-efficiency photocatalysis is obtained.[23] The spectral bands of various active groups, including CO ($b^3\Sigma_{2u}$–$a^3\Pi_{1g}$), CO_2^+ ($B^2\Sigma_u^+$–$X^2\Pi_g$), and CO_2^+ ($A^2\Pi_u$–$X^2\Pi_g$), were detected, as demonstrated in Table S2 and Fig. S7 (ESI†).

The vertical ionization energy of CO_2 stands at 13.77 eV,[24] while exciting CO_2^+ from its $X^2\Pi_g$ state to the $A^2\Pi_u$ and $B^2\Sigma_u^+$ states necessitates energies of 3.54 eV and 4.31 eV, respectively.[25] This indicates that the formation of CO^{2+} in the $X^2\Pi_g$, $A^2\Pi_u$, and $B^2\Sigma_u^+$ states within the plasma relies on the presence of high-energy electrons, as outlined in eqn S5–S7 (ESI†), while the de-excitation of these active species leads to the emission of photons possessing specific energies, as shown in eqn S8 and S9 (ESI†).

The CO yield of the $CsPbBr_3$@ReS_2-15 photocatalysis, ReS_2 plasma catalysis, and plasma photocatalysis of $CsPbBr_3$ and $CsPbBr_3$@ReS_2-15 under the same mass condition was compared. It is observed that the CO yield in the DBD plasma filled with $CsPbBr_3$@ReS_2-15 (4.77×10^6 μmol g^{-1} h^{-1}) is 56.4% higher than that of ReS_2 (3.05×10^6 μmol g^{-1} h^{-1}), and is much larger than the sole photocatalytic process (25.67 μmol g^{-1} h^{-1}) (Fig. 3d). This highlights the superiority of plasma photocatalysis in the CO_2 conversion. Compared with $CsPbBr_3$, the ability of the $CsPbBr_3$@ReS_2-15 heterojunction photocatalyst to absorb light and effectively utilize the photons generated in the DBD plasma is greater, while the presence of a Z-type charge transfer path between ReS_2 and $CsPbBr_3$ suppresses the recombination of charge carriers, thereby improving the overall CO_2 conversion performance.

In summary, $CsPbBr_3$ QDs were grown on ReS_2 to construct the $CsPbBr_3$@ReS_2 heterojunction. The $CsPbBr_3$@ReS_2 photocatalysts show stronger optical absorption and a type-Z heterojunction, and the photocatalytic CO production is 25.67 μmol g^{-1} h^{-1} for $CsPbBr_3$@ReS_2-15. The increase in photocatalytic activity is attributed to the improved light absorption and the formation of a Z-scheme heterojunction, facilitating the spatial separation of photogenerated charge carriers. Moreover, DBD plasma filled with $CsPbBr_3$@ReS_2-15 delivers the optimum CO_2 conversion ratio of 35.60% and energy efficiency of 13.10%. This exceptional performance was obtained due to not only the excellent photocatalytic activity of $CsPbBr_3$@ReS_2-15, but also the increased micro-discharge time and satisfactory discharge uniformity of the DBD plasma. This work will promote the development of plasma photocatalytic CO_2 conversion.

This work was supported by the National Natural Science Foundation of China (No. 22072010), and the Natural Science Foundation of Chongqing Municipality (No. CSTB2024NSCQ-LZX0101).

Data availability

The data supporting this article have been included as part of the ESI.†

Conflicts of interest

There are no conflicts to declare.

Notes and references

1 A. Goeppert, M. Czaun and G. S. Prakash, *et al.*, *Energy Environ. Sci.*, 2012, **5**, 7833–7853.
2 J. Zhou, X. Zha and Z. Chen, *et al.*, *Appl. Catal. B*, 2024, **350**, 123911.
3 T. Tomai, K. Katahira and H. Kubo, *et al.*, *J. Supercrit. Fluid.*, 2007, **41**, 404–411.
4 S. Xu, H. Chen and C. Hardacre, *et al.*, *J. Phys. D: Appl. Phys.*, 2021, **54**, 233001.
5 D. Mei, X. Zhu and Y. L. He, *et al.*, *Plasma Sources Sci. Technol.*, 2014, **24**, 015011.
6 M. S. Moss, K. Yanallah and R. W. K. Allen, *et al.*, *Plasma Sources Sci. Technol.*, 2017, **26**, 035009.
7 S. Renninger, M. Lambarth and K. P. Birke, *J. CO_2* Util., 2020, **42**, 101322.
8 G. Chen, T. Godfroid and N. Britun, *et al.*, *Appl. Catal., B*, 2017, **214**, 114–125.
9 W. Wang, D. Mei and X. Tu, *et al.*, *Chem. Eng. J.*, 2017, **330**, 11–25.
10 Q. Huang, C. Fu and Z. Liang, *et al.*, *J. Phys. Chem. C*, 2023, **127**, 11550–11558.
11 X. Zhu, Y. Lin and J. San Martin, *et al.*, *Nat. Commun.*, 2019, **10**, 2843.
12 A. Kipkorir, J. DuBose and J. Cho, *et al.*, *Chem. Sci.*, 2021, **12**, 14815–14825.
13 J. H. Cho, I. G. Koo and M. Y. Choi, *et al.*, *Appl. Phys. Lett.*, 2008, **92**, 101504.
14 J. G. Gu, Y. Zhang and M. X. Gao, *et al.*, *J. Appl. Phys.*, 2019, **125**, 153303.
15 Q. Huang, J. Yang and F. Qi, *et al.*, *Chem. Eng. J.*, 2022, **437**, 135299.
16 F. Li, X. Yue and Y. Liao, *et al.*, *Nat. Commun.*, 2023, **14**, 3901.
17 Q. Huang, Z. Liang and F. Qi, *et al.*, *J. Phys. Chem. Lett.*, 2022, **13**, 2418–2427.
18 Q. Huang, C. Fu and Y. Shen, *et al.*, *J. Phys. Chem. Lett.*, 2023, **14**, 8922–8929.
19 O. Guselnikova, P. Postnikov and J. Kosina, *et al.*, *J. Mater. Chem. A*, 2021, **9**, 8462–8469.
20 N. Lu, N. Liu and C. Zhang, *et al.*, *Chem. Eng. J.*, 2021, **417**, 129283.
21 X. Tu, H. J. Gallon and M. Twigg, *et al.*, *J. Phys. D: Appl. Phys.*, 2011, **44**, 274007.
22 Y. Cao, W. Yang and W. Zhang, *et al.*, *New J. Chem.*, 2004, **28**, 218–222.
23 A. Zabelina, J. Dedek and O. Guselnikova, *et al.*, *ACS Catal.*, 2023, **13**, 3830–3840.
24 O. Alwan, O. Chuluunbaatar and X. Assfeld, *et al.*, *J. Phys., B*, 2014, **47**, 225201.
25 M. A. Johnson, R. N. Zare and J. Rostas, *et al.*, *J. Chem. Phys.*, 1984, **80**, 2407–2428.